A Natural State and Production Forecast Model of the Salton Sea Geothermal Field for Lithium Extraction

John O'Sullivan[1], Naod Araya[2], Joris Popineau[1], Theo Renaud[1], and Jeremy Riffault[1]

University of Auckland[1], Ormat Technologies[2]

Keywords

Numerical Models, Leapfrog Geothermal, Natural State, Forecast, Salton Sea, Lithium

ABSTRACT

The Salton Sea Geothermal Field is a significant geothermal resource with an estimated resource potential of nearly 3 GW (Kaspereit et al., 2016). In addition, its geothermal brine is highly enriched in lithium and other valuable metals (McKibben et al., 2021). Historically, this high salinity and metal rich fluid chemistry as well as partial coverage by the Salton Sea limited exploitation. However, recent developments in direct lithium extraction and renewable energy goals have renewed stakeholder interest in the field.

A robust and integrated numerical model is needed to facilitate sustainable extraction of the field's lithium and geothermal energy. This modeling study seeks to build upon pervious conceptual and numerical modeling work of the SSGF to characterize and forecast the field's recoverable lithium potential.

Araya and O'Sullivan (2022) natural state model was upgraded to include chloride and CO_2 in the equation-of-state and lithium as a passive tracer. The natural state model was then recalibrated using measurements of the chloride distribution as well as the pre-development temperature distribution in the system. The re-calibrated model was able to reproduce a deep hypersaline reservoir overlaid by a mixing zone and a low-salinity shallow zone. A dual-porosity production model was then created and calibrated using publicly available production data. This data included production and reinjection rates and chloride concentrations.

A future scenario was run to estimate the effect of lithium extraction on lithium production rates. Lithium production rates are forecast to decline as a result of chemical breakthrough of reinjection fluid with a low concentration of lithium. The rates of decline are dependent on the connectivity between production and reinjection wells and can be optimized through careful planning of reinjection strategies. Greater grid refinement, improved model calibration and uncertainty quantification can improve the model to provide more accurate and robust forecast scenarios.

1. Introduction

1.1 Background

The Salton Trough is an active pull-apart basin straddling the Pacific and North American Plates in Southern California. This continental rift zone is characterized by a series of right-stepping dextral faults that link the East Pacific Rise to the San Andreas fault system (Dorsey, 2006). In the extensional gaps between these step-over faults there are a series of smaller spreading centers bounded by northwest-trending strike-slip faults and northeast-trending normal faults (Hulen et al., 2002).

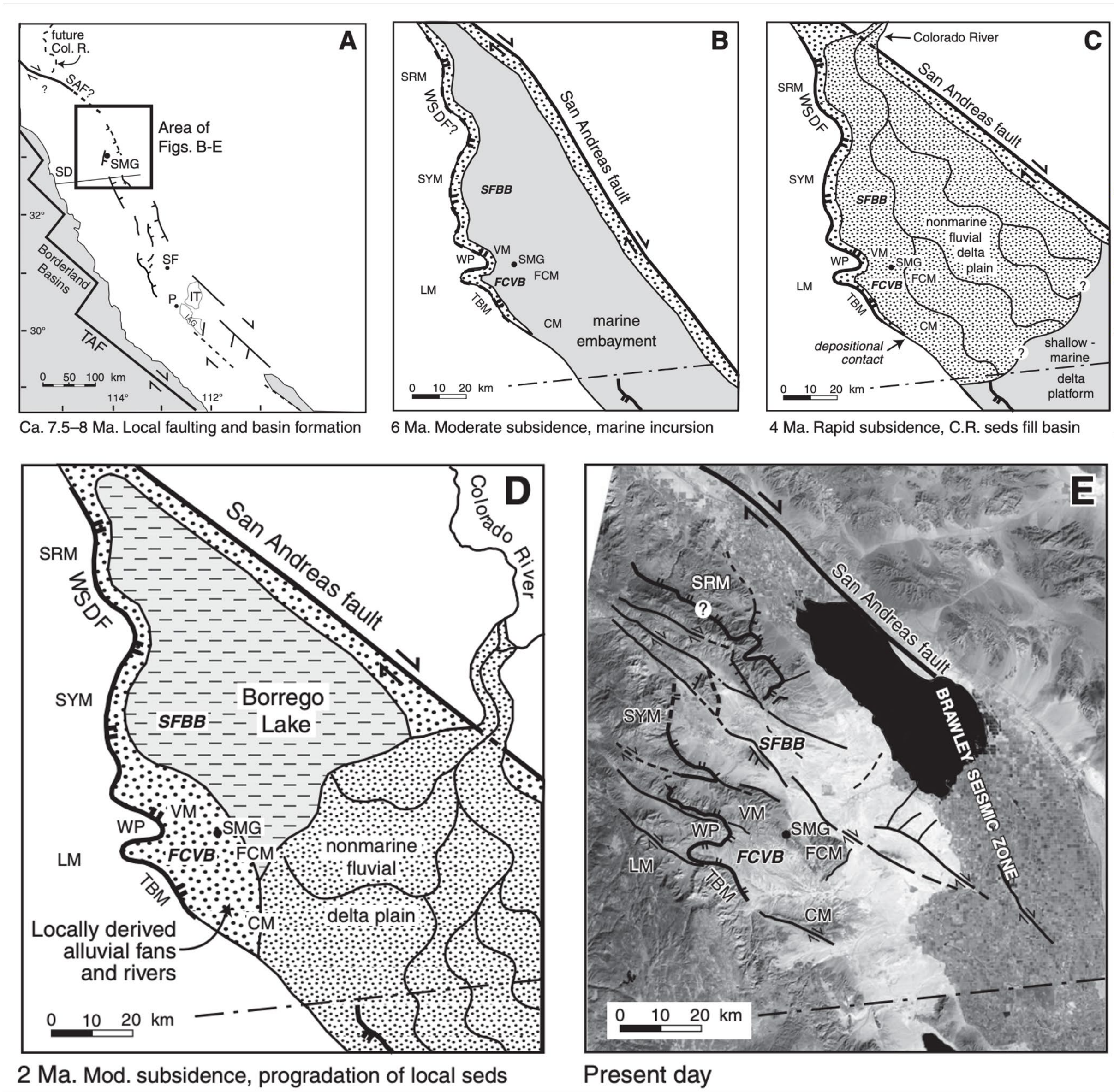

Figure 1. Paleogeographic reconstructions of the Salton Trough and surrounding region at 7.5–8, 6, 4, and 2 Ma by Dorsey et al., 2011.

1.2 Sedimentation History

Since the onset of subsidence at ca. 8.5-7 Ma, nearly continuous deposition has filled the Trough with more than 6 km of marine, deltaic, alluvial, and lacustrine sediments (Dorsey et al., 2011). The late Miocene was marked by moderate crustal thinning and basin subsidence which resulted in a deep marine incursion into the Salton Trough. The Imperial Group, a thick marine transgression of fossiliferous claystone and siltstone, was deposited during this time (Dorsey et al., 2011). During a period of increased subsidence in the Pliocene, the nascent Colorado River began depositing a large volume of fluvial sediments into the northern portion of the Trough. The delta plain was characterized by avulsing channels and flood plains that quickly prograde southwards (Dorsey et al., 2011). This period corresponds with the thick arkosic sandstone and intermittent argillaceous intervals of the Palm Springs Formation (Dorsey, 2006). By 2 Ma, right lateral motion on the San Andreas Fault moved the exit point of the Colorado River south of the contemporary Salton Sea (see Figure 1.D). This southward migration of the exit point led to the southward expansion of the perirenal Borrego Lake. This changing environment correlates with the thick claystone, siltstone, and fluvial sandstone lens of the Borrego Formation (Dorsey, 2006). During the early Pleistocene to Holocene the Colorado River would alternate its flow direction resulting in repeated flooding and drying cycles of paleolake Cahuilla (McKibben, 1991). This period corresponds with the development of the Brawley Formation of lacustrine mudstone and evaporitic deposits that serves as the impermeable cap to geothermal fluids (Helgeson, 1968).

1.3 Magmatism and Metamorphism

Due to crustal thinning and deep magmatic intrusions, the entire Salton Trough experiences an abnormally high heat flux of >100 mW/m^2 (Lachenbruch et al., 1985). Even higher heat flows of >500 mW/m^2 are concentrated in Salton Sea Geothermal Field due to localized Quaternary volcanism and upwelling of hydrothermal fluids (Sass et al., 1984). As a result, significant metamorphic and hydrothermal alteration of the Colorado River sediment occurs at shallower depths in the SSGF (~1.5 km) compared to the rest of the valley (~3 km) (Han et al., 2016).

1.4 Brine Chemistry

The brine of the Salton Trough is distinguished by a bimodal distribution of salinity. Cooler less saline brine (<10 wt.% TDS) overlays hot hypersaline brine (>20 wt.% TDS). The hypersaline brines tend to be Na-Ca-K chloride solutions with high concentrations of dissolved metals (Fe, Mn, Zn, Li, Sr) while the less saline brines are typically NaCl solutions with very little dissolved metals (McKibben et al., 1987). McKibben et al. 2021 notes that metal concentrations in the reservoir brines varies linearly with the chlorine concentrations (Figure 2). The hypersaline brines are highly enriched in lithium >200ppm compared to the reservoir rocks which have an average concentration of 40ppm. This suggests that the bulk of the recoverable lithium resource currently resides within these hypersaline brines rather than in the rocks (McKibben et al., 2021).

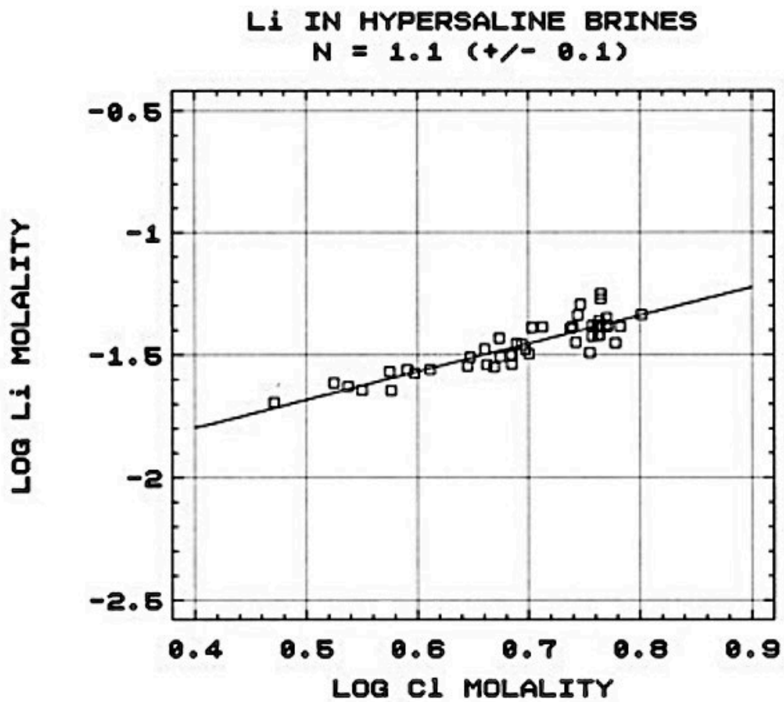

Figure 2. Variation of dissolved and lithium (Li) metal content (in molality: moles of metal per kilogram of brine) as a function of the brine’s chlorinity (dissolved chlorine molality) in Salton Sea Geothermal brines (McKibben et al., 2021).

These hypersaline brines are thought to have originated from Pleistocene era partially evaporated Colorado River water. As this brackish water seeped deep into the sedimentary basin, it was heated up causing more minerals and metals to dissolves out of the reservoir rocks and into this now deep aquifer (McKibben and Hardie, 1997). Lastly, the narrow range of isotopic compositions of these deep brines indicates active convection and a relatively long residence time (Williams and Mckibben, 1989).

2. Conceptual Model Review

Modeling concepts and workflows described by O’Sullivan et al. (2000), O’Sullivan et al. (2016), and Popineau et al. (2018), as well as Leapfrog Geothermal software, were used to create a combined geology, alteration, and structural model.

2.1 Geological Model

Based on previous work by Wagoner (1980), Dorsey (2006), Dorsey et al. (2011), Kirby et al. (2007), and Hulen et al. (2003), the following seven geologic units were modeled chronologically from oldest to youngest: Crystalline Basement, Imperial Group, Palm Springs Formation, Lower Borrego, Upper Borrego, Brawley Formation, and Alluvium. Regional stratigraphic cross-sections from these studies were used to establish the general thickness of each formation. The Borrego Formation was split to capture the dramatic metamorphic and seismic velocity changes that occur at ~1.5 km depths beneath the center of the SSGF. The crystalline basement surface contact was traced using a regional geological map (California Department of Conservation, 2015).

2.2 Structural Model

The Salton Sea sub-basin is dominated by a complex network of blind right-stepping dextral faults and R' Riedel shear faults. The modeled dextral faults include the left strand of the Brawley Fault Zone (fault I), the right strand of the BSZ (fault B), Red Hill (fault R), Calipatria (fault P), Wister (fault W), Southern San Andreas (fault A) and fault C which was inferred from the alignment of old CO_2 fumaroles and wells (e.g., Svensen et al., 2007; Mazzini et al., 2011; Rao, 2016). These faults were all modeled as having near-vertical dips. They were digitized from maps provided by Kaspereit et al. (2016), Marshall et al. (2022), and Lynch and Hudnut (2008). Some liberties were taken with their ultimate placement and orientation (Figure 3).

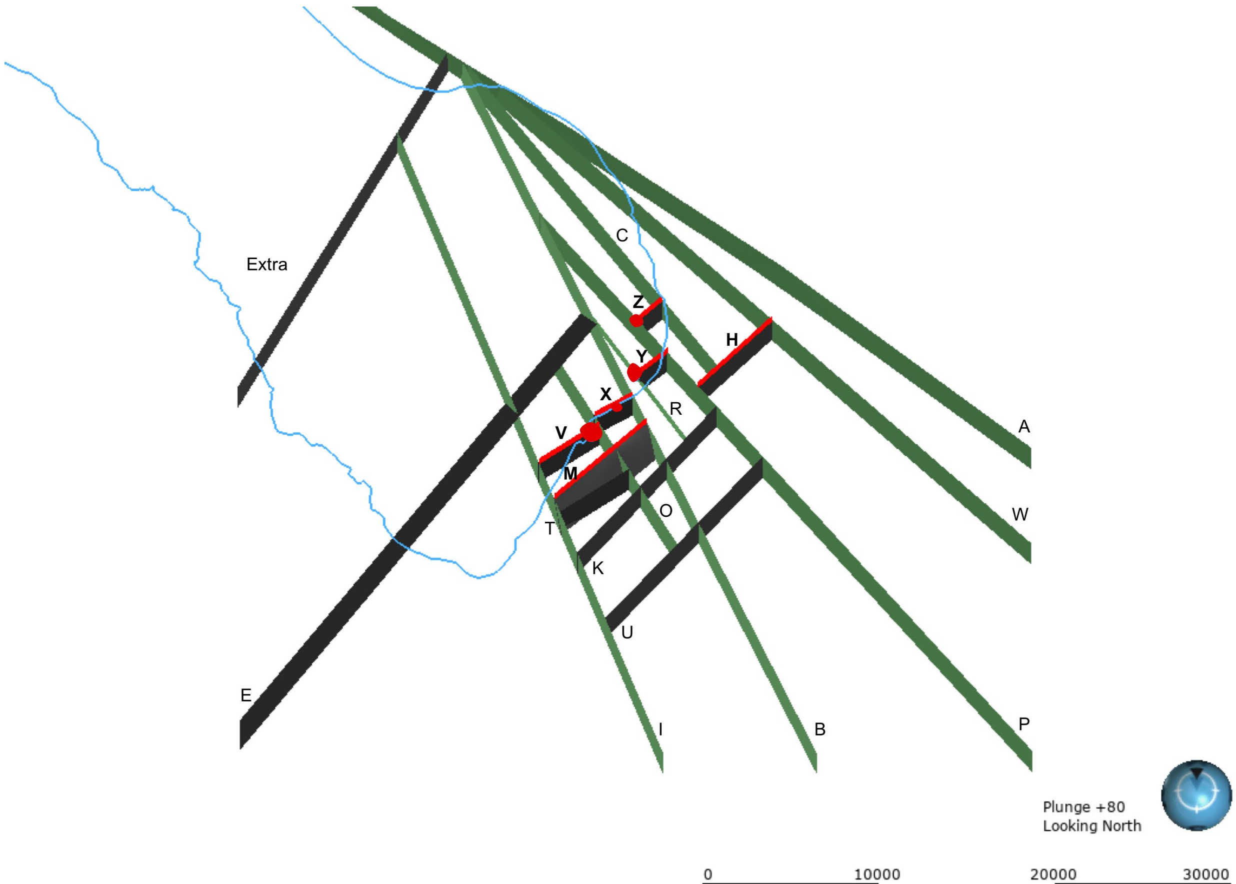

Figure 3. Input faults into the numerical model. Salton Sea (light blue) and volcanic buttes (red) as reference. Green faults are the near vertical dextral faults. Black faults are R' faults with little to no upwelling. The black faults with red traces represent R' faults with significant upwelling (Araya and O'Sullivan, 2022).

The previously mentioned fault maps in addition to one from McGuire et al. (2015) were used to digitize the R' Riedel shear faults. These faults include the Elmore Ranch (fault E), Main Central Fault Zone (fault M), Kalin (fault K), Hudson (fault H), Southern boundary (fault U), fault T, Butte 1 (fault V), Butte 2 (fault X), Butte 3 (fault Y), Butte 4 (fault Z).

2.3 Clay Cap

Four 2D land and offshore resistivity profiles by Nichols (2009) were used to digitally construct the clay cap in the conceptual mode. The clay cap was defined as the extremely conductive zone (0.2 to 0.4 Ohm-M). Some uncertainty in the location of the clay cap exists as the combination of high temperature, high salinity, and high porosity can also produce very low resistivity values (Nichols, 2009). The landward lateral extent of the clay cap was further refined by resistivity and density maps from Younker et al. (1981). Due to the lack of 3D MT data, modeler discretion was used thereby increasing the potential uncertainty in model parameters.

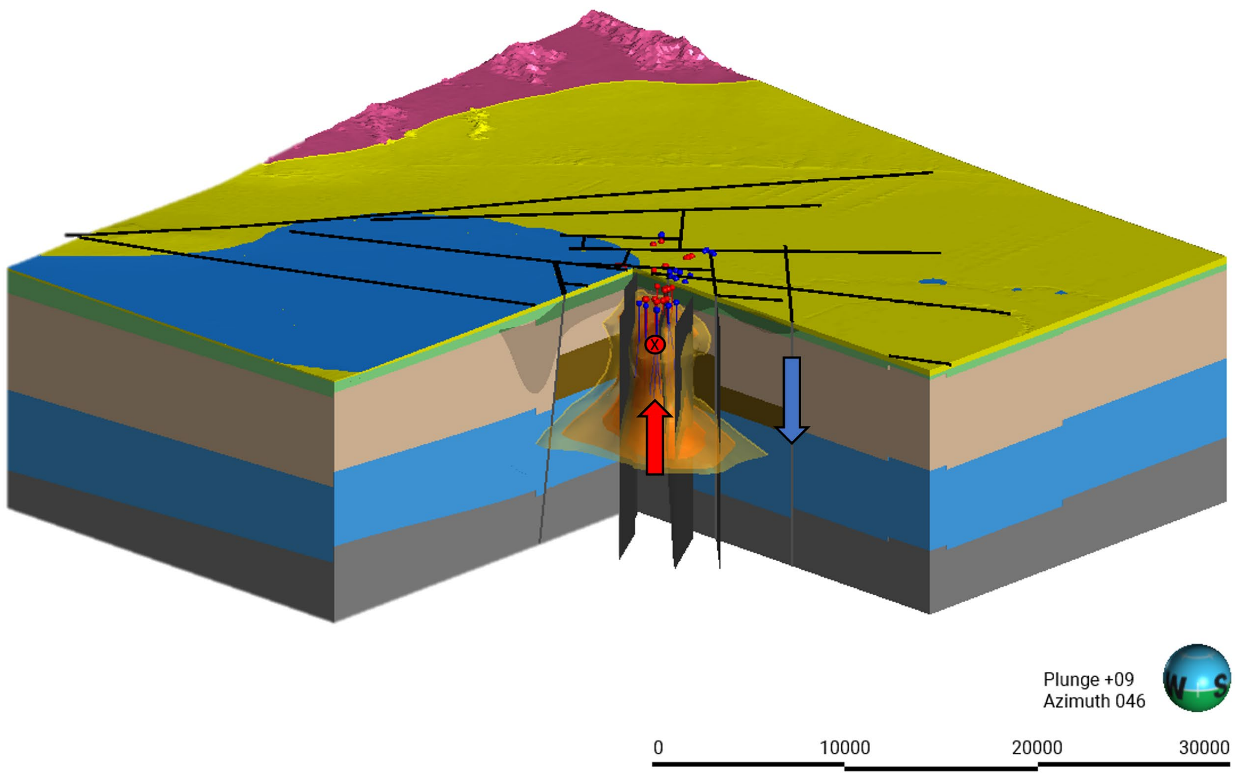

Figure 4. Conceptual model of the Salton Sea Geothermal Field. Salton Sea (blue). Geological units: Granitic Basement (pink), Imperial Formation (grey), Palm Springs (blue), Upper Borrego (tan), Lower Borrego (brown), Brawley (Green), Alluvium (yellow). Select faults shown as black surfaces. Fault traces (black). Shaded zone denotes clay cap. Active production wells (red). Active injection wells (blue). Red arrows show upflow and blue arrows show cold down flow.

3. Updated Numerical Reservoir Model

Numerical models are used to simulate the natural state (pre-production) of hydrothermal systems as well as their production history and future behavior in response to utilization. Physical laws such as conservation of mass and energy as well as Darcy's Law are used to mathematically simulate hydrothermal flow through a porous, fractured, and heterogeneous subsurface media. Through this workflow, geothermal reservoir simulation and its calibration to field data are powerful instruments that allow for a robust 3D characterization of subsurface permeability, porosity, heat, and mass input parameters. This study followed the modeling framework established by O'Sullivan et al. (2023).

The 3D conceptual model was discretized into a block model in order to apply mass and energy balance calculations using the Waiwera geothermal simulator (Croucher et al., 2020). The model was run in Amazon Web Services (AWS) Cloud using 96 core high-performance compute nodes.

A grid extending 24 x 24 x 3.5 km and oriented along the NE trending axis of the Main Central Fault Zone was created in Leapfrog Geothermal. The grid has a 400 x 400 m lateral refinement within the SSGF boundary and an 800 x 800 m refinement on the periphery. The grid was designed with a vertical refinement of 25 m near the surface, 50 m at the water table, 100 m in the upper reservoir, 200 m in the lower reservoir, and 500 m at the greatest depths (see Figure 5). Greater vertical refinement in the shallow zone allows the model to better capture the steep temperature gradients that occur in this zone. The final numerical grid consisted of 37,688 blocks.

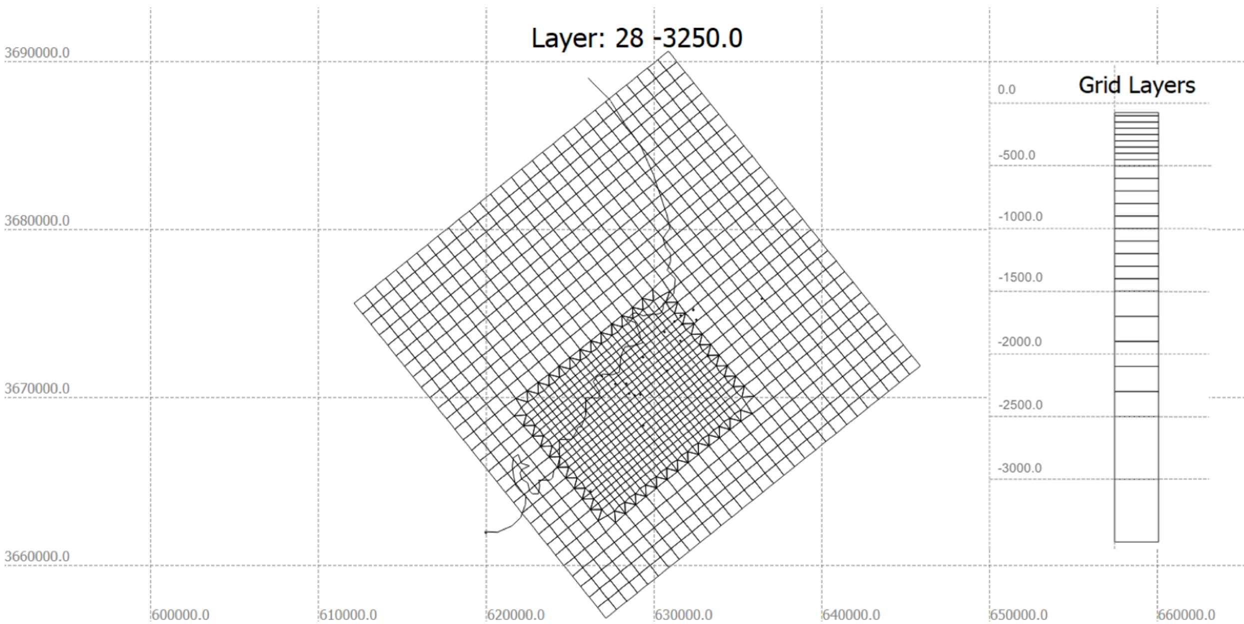

Figure 5. Map view of the numerical grid with black line representing the Salton Sea shoreline. The cell size in the refined area of the grid is 160,000 m^2, and in the coarser area it is 640,000 m^2. The thickness of the grid layers increases with depth.

Waiwera's "wsce" (Water, Salt, CO_2, Energy) equation of state was used to include salinity and CO_2 in the thermodynamic calculations and lithium was included as a passive tracer. The top of the model was assigned dry atmospheric conditions of 1 bar and a mean temperature of 23°C on land and a wet atmosphere for the Salton Sea with a temperature of 23°C and a pressure determined by the depth of the sea. The chloride concentration of the Salton Sea was set to a mass fraction of 50,000 ppm. The side boundaries of the grid are located past all bounding faults allowing no-flow lateral boundary conditions to be applied following best practice suggested by O'Sullivan et al. (2000). At the base of the model a background heat flux of 150 mW/m^2 was applied with an additional 136 MW applied as heat and mass inputs under the SSGF representing the deep geothermal upflow. Chloride was included in the deep upflow at a mass fraction equivalent to 152,000 ppm and lithium at a concentration of 220 ppm, a ratio of 682:1. The CO_2 concentrations were fixed at negligible values for all boundary conditions during this stage of the project.

The model used 561 rock-types covering the combinations of lithology, fault zone, fault zone intersections, and alteration included in the conceptual model. This exhaustive use of rock-types ensured that the numerical model lithology, alteration, and structural controls robustly mirror the current conceptual model understanding of the SSGF. Many of the rock-type classifications share common permeability and porosity values, but the large number of combinations allows a high level of heterogeneity in the permeability and porosity distributions as required. Other secondary rock properties (density, heat conductivity, and rock grain-specific) were held constant across all rock-type classifications.

During production and future scenario runs, a dual-porosity model was used to capture reinjection returns more accurately. The dual-porosity parameters are given in Table 1 below.

Table 1: Rock Properties of Major Lithology units

Parameter	Value
Number of matrix blocks	2 (20% and 77.5%)
Volume fraction of fracture blocks	2.5%
Fracture spacing	25 m
Fracture planes	3
Permeability of matrix	1.0E-16 m^2
Permeability of fractures	Variable
Porosity of fractures	80 %

4. Calibration Data

4.1 Exploration Wells

Static temperature and brine chemistry data from exploration wells drilled prior to the start of 1980s commercial production were compiled from studies by Helgeson (1968), Palmer (1975), and Sass et al. (1988). Helgeson (1968) obtained temperature measurements over a three-year period for the following eight wells: IID 1, IID 2, IID 3, River Ranch 1, Sinclair 3, Sportsman 1, Elmore 1, and State 1. Palmer (1975) compiled temperature and brine chemistry data from MagMaMax 1, MagMaMax 2, MagMaMax 3, and Woolsey 1. Lastly, Sass et al. (1988) analyzed temperature data from the State 2-14 well to construct an equilibrated static temperature profile.

Static temperature surveys for Lander 2, Elmore IW-4, River Ranch 17, Fee 5, and Vonderahe 1 were collected from CalGEM's GeoSteam data repository. Most of these temperature profiles exhibit a change from a conductive to a convective gradient between depths of 600 to 900 m. This break corresponds well with the average depth of the impermeable clay cap (Sass et al., 1988). Examples of the downhole temperature data are shown in the plots in Figure 6.

4.2 Active Production and Injection Wells

CalGEM's GeoSteam database was used to obtain monthly production and injection data for all the active production and injection wells in the SSGF. These monthly production/injection reports document the average monthly TDS, discharge temperature, wellhead pressure, steam mass rate, and brine mass rate. The GeoSteam database was also used to get well schematics, directional surveys, mud logs, static PTS logs, and well history reports for all the active production and injection wells. Well schematics provided wellhead coordinates, KB, ground level, and total measured depth. Total and/or partial circulation zones that were noted in the mud logs were used to infer feed zones. This was the best approach given the lack of proprietary well-testing and feed zone data. Examples of the production and injection data are shown in the plots in Figure 9 and 10.

5. Natural State Model

The natural state model was calibrated following standard practice by adjusting the permeability distribution and deep geothermal inputs at the bottom boundary of the model. A good model calibration (Araya and O'Sullivan, 2022) had already been achieved matching measured downhole temperatures. However, the addition of chloride significantly affected the thermodynamics of the system requiring substantial re-calibration of the enhanced model.

The plots in Figure 6 show a representative selection of modeled natural state downhole temperatures compared with measured data. While overall there is a good match, more calibration work is required to match the deep isothermal temperature gradients. These deep temperatures reach 360°C which is the limit of application for the current version of Waiwera.

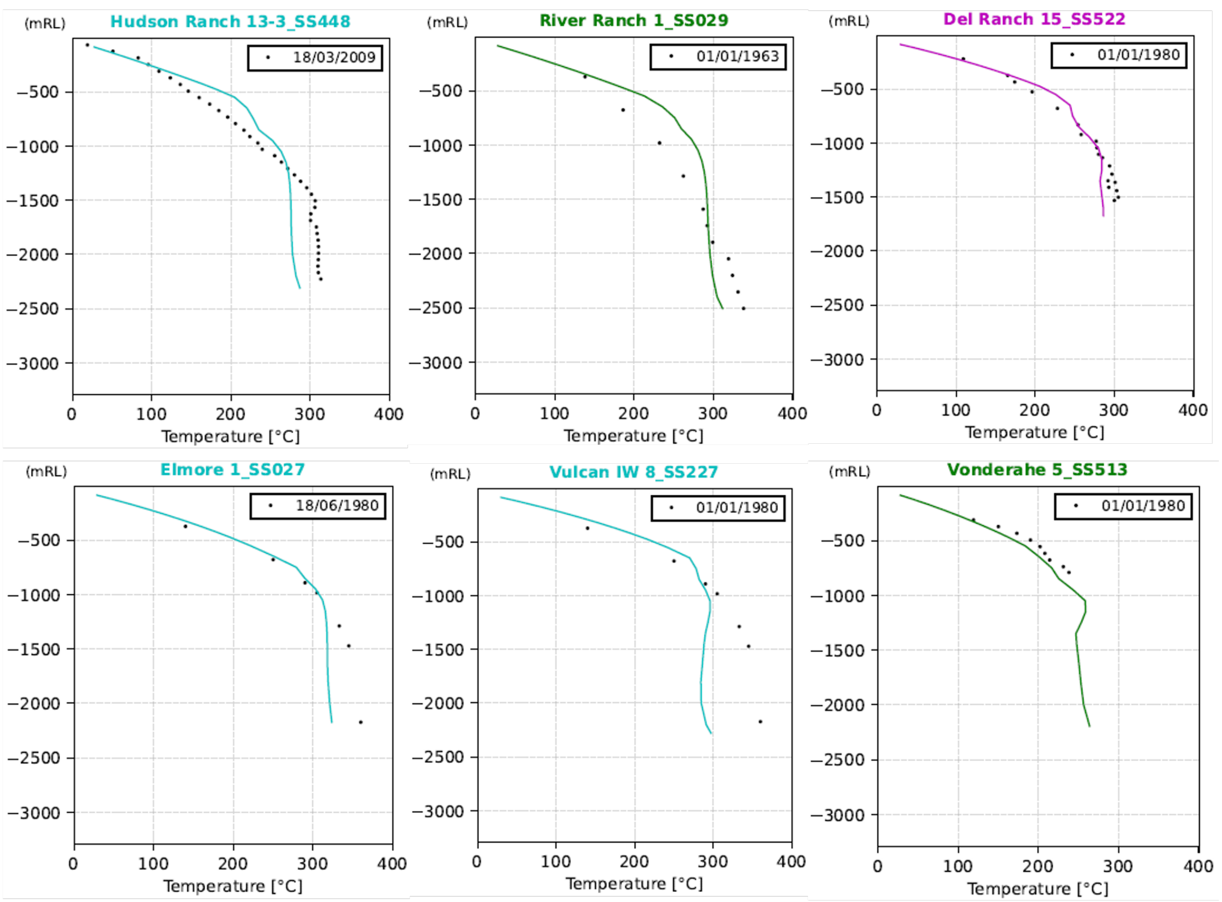

Figure 6. Natural state downhole temperatures for selected wells. Model results are shown as colored lines and measured data as points.

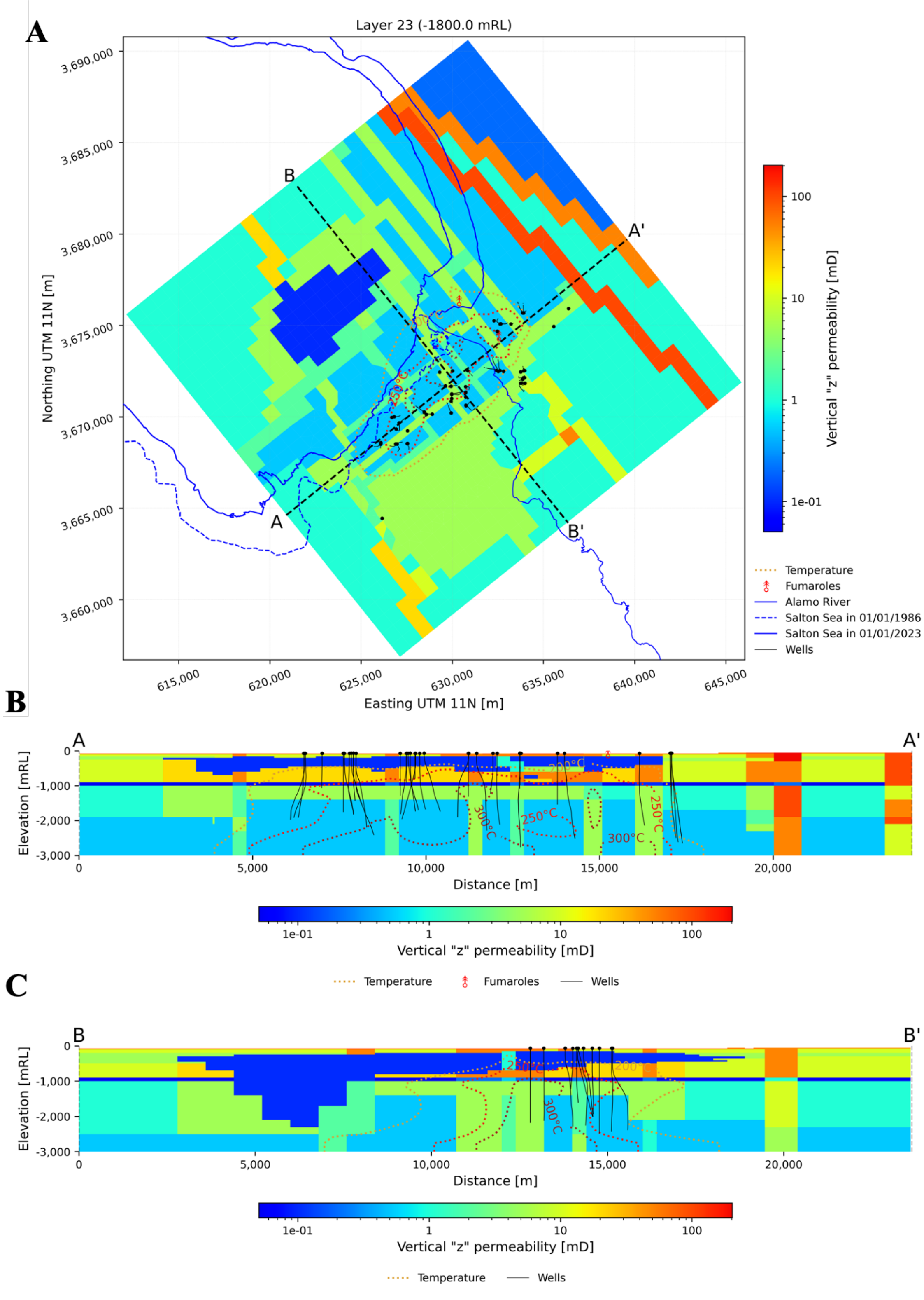

Figure 7. Vertical permeability distribution of model. 300°C, 250°C, and 200°C isotherms shown as maroon, red, and orange dotted lines, respectively. Well tracks (black). A) Horizontal slice at -1800 mRL with A to A' and B to B' slice locations. B) A to A' vertical slice. C) B to B' vertical slice.

Results from the calibration process demonstrate that the infield R’Riedel shear faults and dextral strike slip faults are the main drivers of vertical upflow (see Figure 7). Hot upflow is concentrated along faults M, V, X, Y, O, and I. The reservoir is bounded in the k_1 horizontal direction by faults E, T, K, and U. These R’ shear faults limit outflow to the south and to the northwest. The reservoir is bounded in the k_2 horizontal direction mainly by faults I, O, B, P, W, and A. The clay cap acts as an upper boundary to vertical fluid flow. The clay cap is thickest in the NW of the Sea where it acts as a lateral boundary to northeast outflow. Lastly, the periphery dextral faults (U, K, W, and A) act as large conduits for cold shallow infiltration.

As well as calibrating the temperature distribution, the model permeability distribution was adjusted to produce a chloride distribution consistent with the measured data. In particular, the aim was to reproduce the deep hypersaline reservoir overlaid with an intermediate mixing zone and a low-chloride shallow zone. Figure 8.A shows the 140,000-ppm chloride isosurface from the natural state model. Overall, it captures the deep hypersaline reservoir and the intermediate mixing zone. However, in the model the deep hypersaline fluid penetrates the shallow zone over a much larger area than has been observed. More model calibration is required, reducing permeabilities in the vertical pathways between the deep reservoir and the shallow system to reduce the upflow of hypersaline fluid. Lithium is included in the natural state model as a passive tracer with its concentration coupled closely to chloride concentration. Therefore, the lithium distribution estimated by the natural state model closely follows the chloride distribution as shown in Figure 8.B.

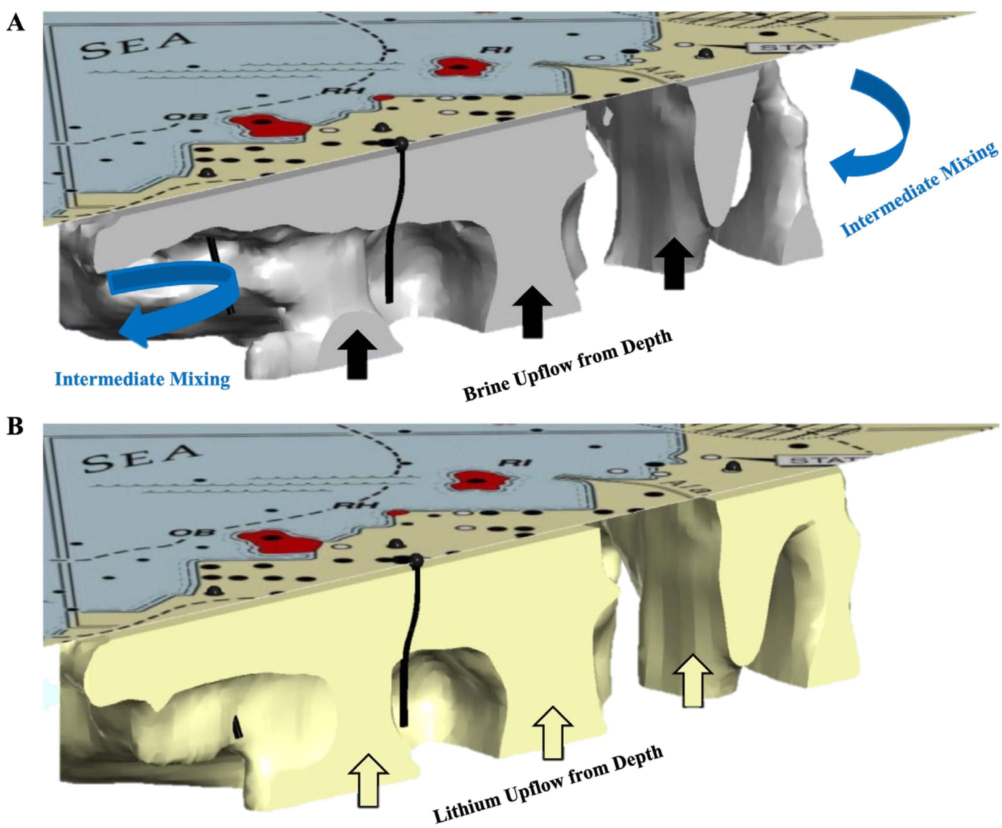

Figure 8. A) Natural state model estimated 140,000 ppm chloride isosurface. B) Estimated 170 ppm lithium isosurface.

6. Production Model

The production model uses the calibrated natural state model as its initial condition and has the same background mass and heat fluxes. It was set up using our standardized framework for including production and reinjection wells (O'Sullivan et al., 2023). This approach adds wells as time dependent source and sink terms in the model blocks corresponding to the feed zones of the production and reinjection wells. The model was then run for the corresponding production history time period and calibrated to match measured transient data for production enthalpies and chloride mass fractions. For the reinjection wells the enthalpy of the reinjected fluid and its chloride concentration are model inputs taken from measured data. The lithium concentration for the reinjection fluid was assumed to remain constant at a ratio of 682:1 to the measured chloride, as no appreciable lithium has historically been extracted from the brine.

Examples of measured data and production model results for selected production and reinjection wells are shown in Figures 9 and 10. Each figure has a map in the upper left showing the location of the well. The results for the production well are typical with the measured chloride concentration increasing over time and a gentle decline in production enthalpy.

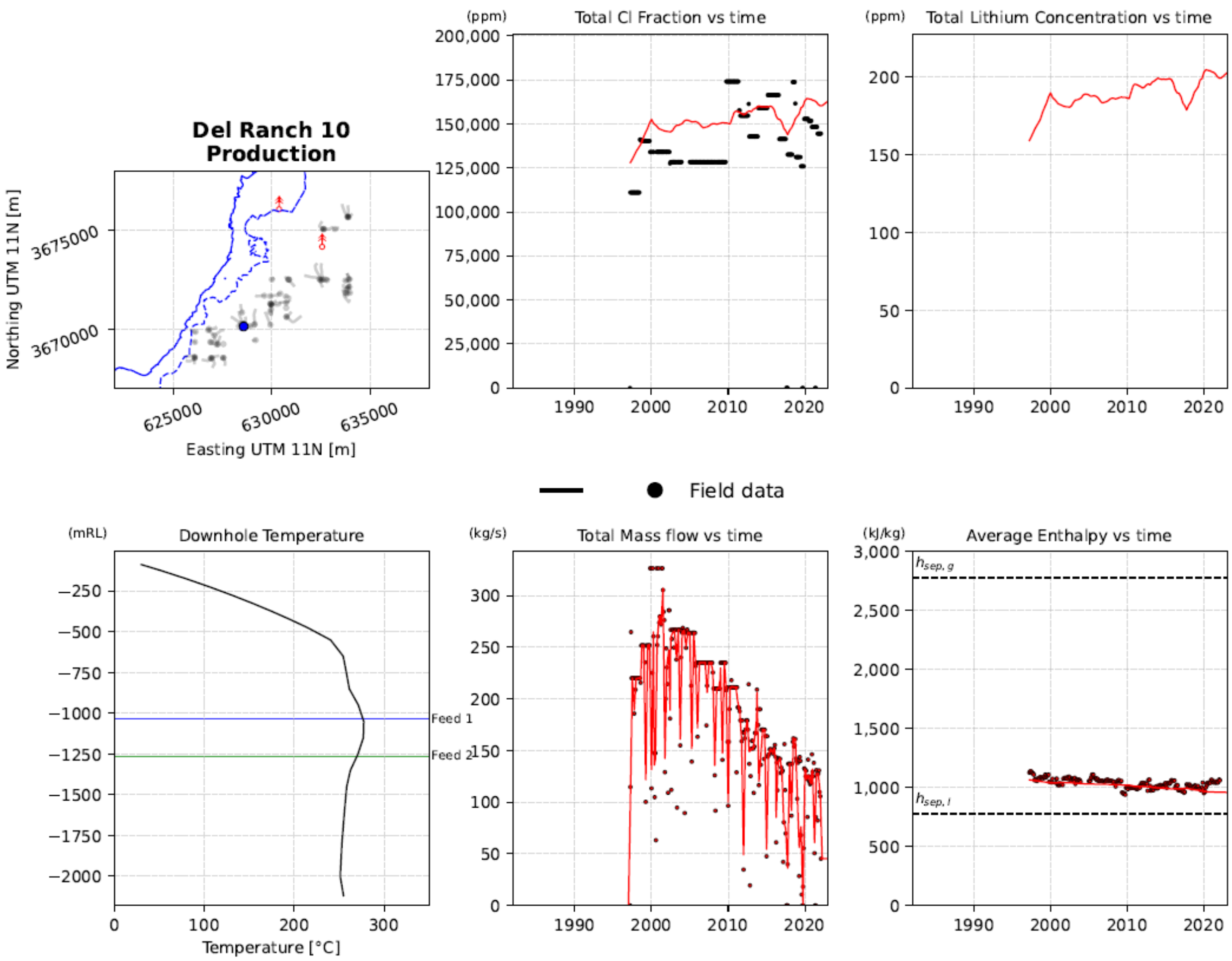

Figure 9. Production model results (solid lines) and measured data (points) for the Del Ranch 10 production well. The location of the Del Ranch 10 well is shown in blue in the map (top left) with the Salton Sea

coastline (original as dashed line, current as solid line) and surface features locations indicated with red markers.

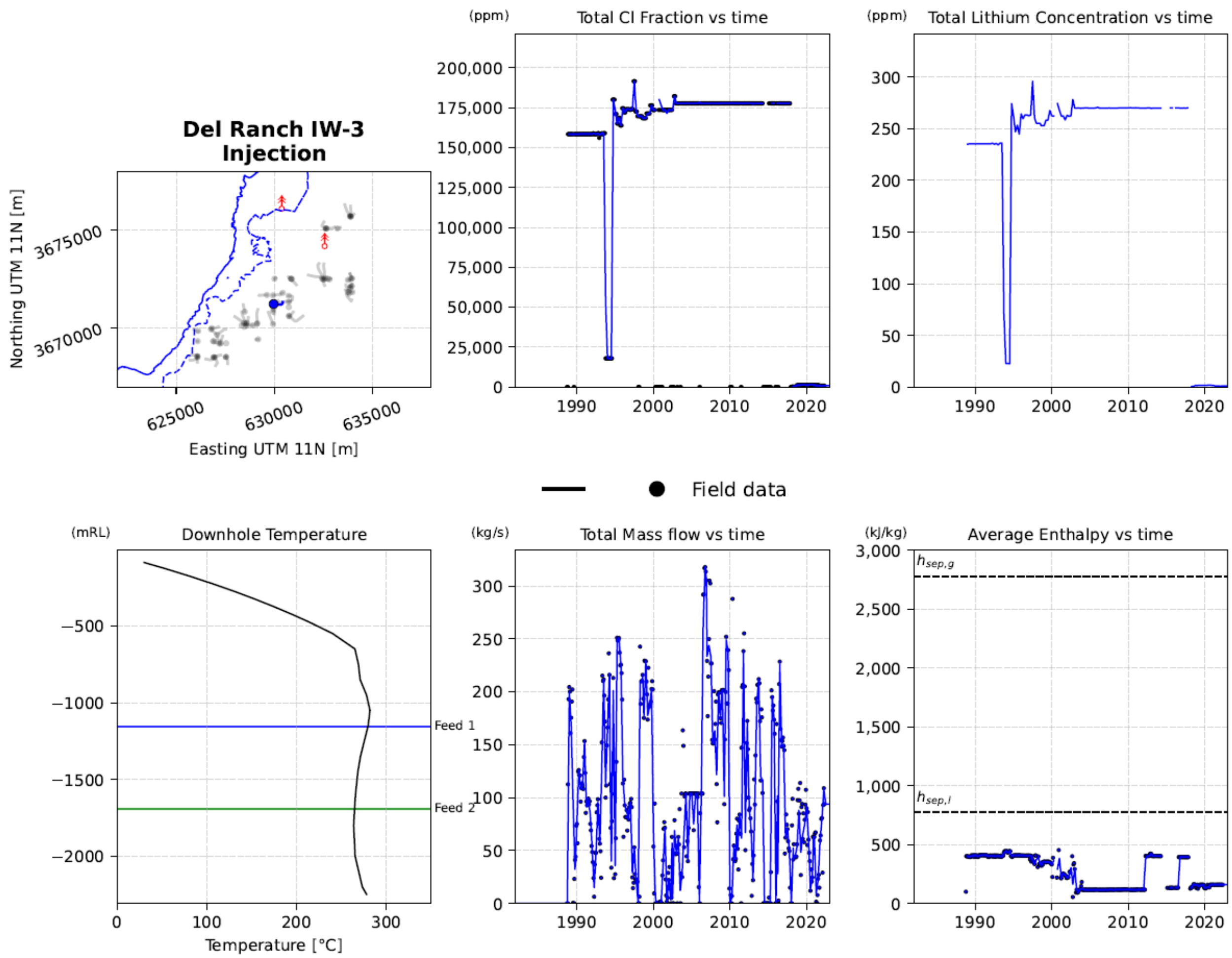

Figure 10. Production model results (solid lines) and measured data (points) for a selected reinjection well. The location of the Del Ranch IW-3 well is shown in blue in the map (top left) with the Salton Sea coastline (original as dashed line, current as solid line) and surface features locations indicated with red markers.

The plots in Figures 9 indicate breakthrough of the higher chloride concentration and lower enthalpy reinjection fluid (see Figure 10). The model results for the selected production well match the measured data very well capturing an increasing lithium production concentration due to the higher lithium concentration in the reinjected fluid than in the reservoir. The good match to the measured data was achieved by calibrating the model's permeability and porosity distribution and the distribution of the upflow of deep, chloride and lithium-rich geothermal brine. The good match that is also achieved for the production enthalpy further demonstrates that the model calibration represents the permeability and porosity distribution well. Further calibration could still improve the model's match to the data for the well shown in Figure 9 reducing the enthalpy decline in the model slightly by reducing the connectivity between this well and nearby injectors. Similarly, the match to other production wells can be improved with more calibration though the current calibration is sufficient to draw preliminary conclusions given the uncertainty in the available data.

The rate of thermal and chemical breakthrough as a result of reinjection is dependent on the permeability and porosity distributions, the location of the production and the reinjection wells and their feedzones, and the rates of production and reinjection. Figure 11 shows the model representation of the chloride distribution at 2023 as a result of 40 years of geothermal production and reinjection. It shows that the increased chloride concentrations are distributed heterogeneously across the field as a result of faults, formations and differences in production and reinjection elevations. The current model does a good job of matching the overall behavior of the SSGF and the dual-porosity approach allows a good representation for the reinjection returns. However, more calibration, more detailed calibration data and a more refined model grid would allow for more accurate representation of the historic changes in the chloride and lithium concentrations.

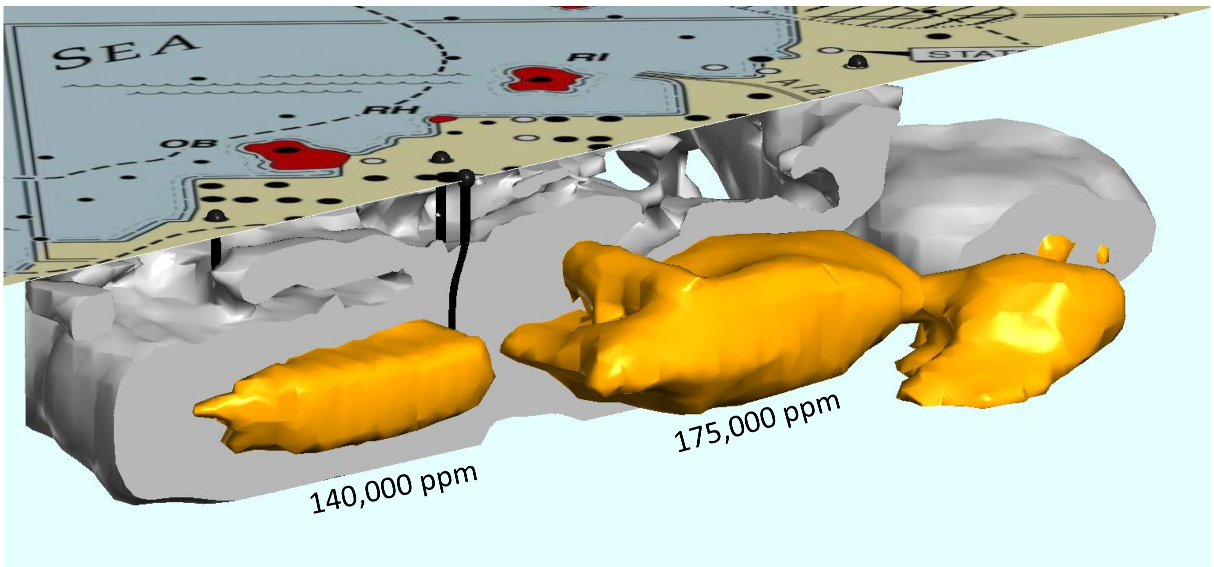

Figure 11. Chloride isosurfaces at 2023 estimated from the production model. The 140,000 ppm isosurface is cut away to reveal the 175,000 ppm isosurface.

7. Lithium Forecast Scenarios

At this stage of the project a simple future scenario was defined to investigate the broad effect of lithium extraction on lithium production rates. The scenario assumed that all production and reinjection rates remain constant for all wells for the next 20 years. The reinjected chloride concentrations also remain constant for the full period. However, from 01/01/2024 the lithium concentration for all reinjection wells was reduced by 95%, which is representative of a future scenario where technology allows for 95% of the lithium in the brine to be extracted before reinjection. An example of the input data for a selected reinjection well is shown in Figure 12.

Production concentrations of lithium for all production wells were calculated with examples shown for two selected wells in Figure 13. The total amounts of production and reinjection as well and the total amount of lithium produced and reinjected are shown in Figure 14. These figures show a general decline in forecasted lithium production because of chemical breakthrough from the reinjected fluid with a low lithium concentration. The plot in Figure 15 shows the final distribution of lithium with the lower 100 ppm concentration isosurface forming a bubble around the central production and reinjection wells. However, the results in Figure 13 show that the effect can be quite different depending on which production well is considered. Del Ranch 10 production well is forecast to experience rapid decline in lithium production due to its proximity and connectivity to nearby reinjection wells. Whereas PW Hudson Ranch 13 is forecast to have relatively stable lithium concentrations through the 20-year scenario.

These results show that the details of the connectivity between production and reinjection wells are important for determining lithium production rates. This has two important implications. First, it is important to model the connectivity between production and reinjection wells as accurately as possible and account for uncertainty in the model forecasts. And second, the lithium production rates can be manipulated and optimized by planning targeted reinjection.

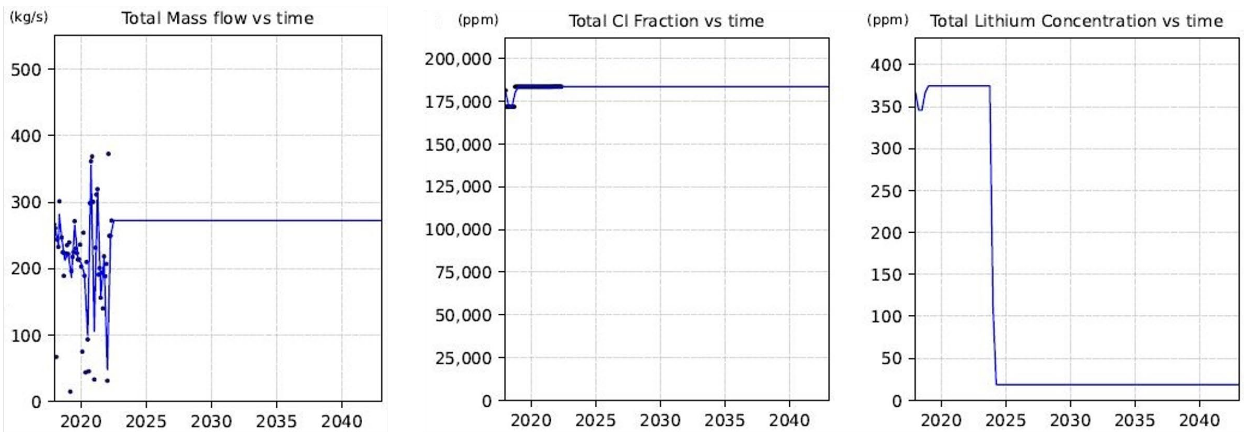

Figure 12. Future scenario model results (solid lines) and measured data (points) for a selected reinjection well.

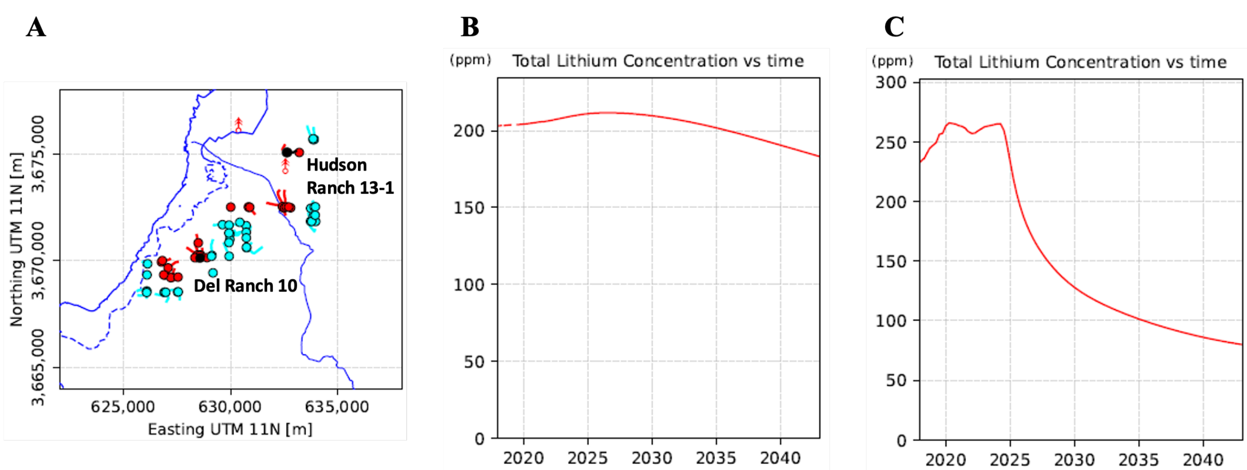

Figure 13. A) Well locations shown on map in black. Other production well locations shown in red and reinjection wells in cyan. Future scenario model results for B) Hudson Ranch 13-3 C) Del Ranch 10.

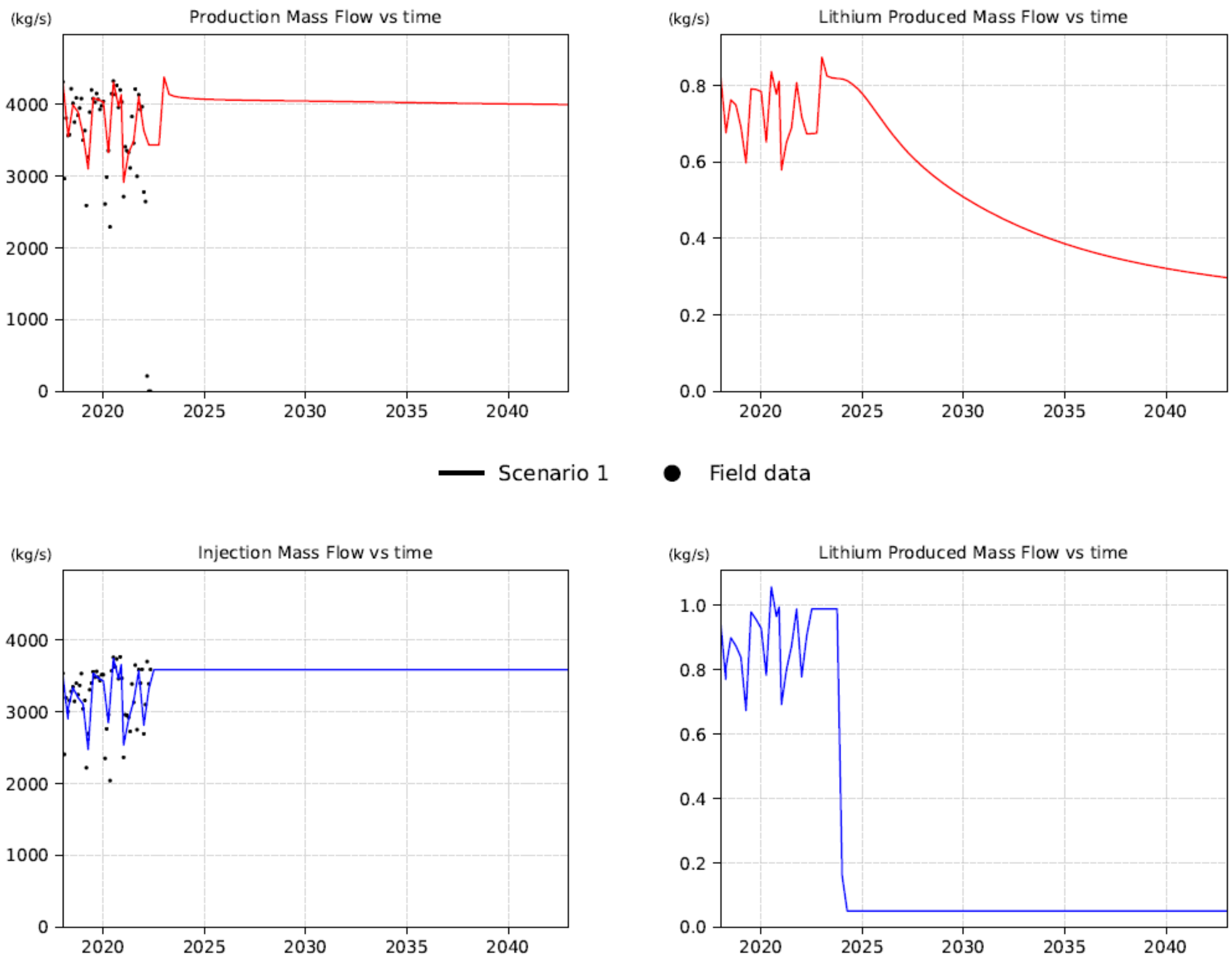

Figure 14. Future scenario model results of totals for all production and reinjection wells.

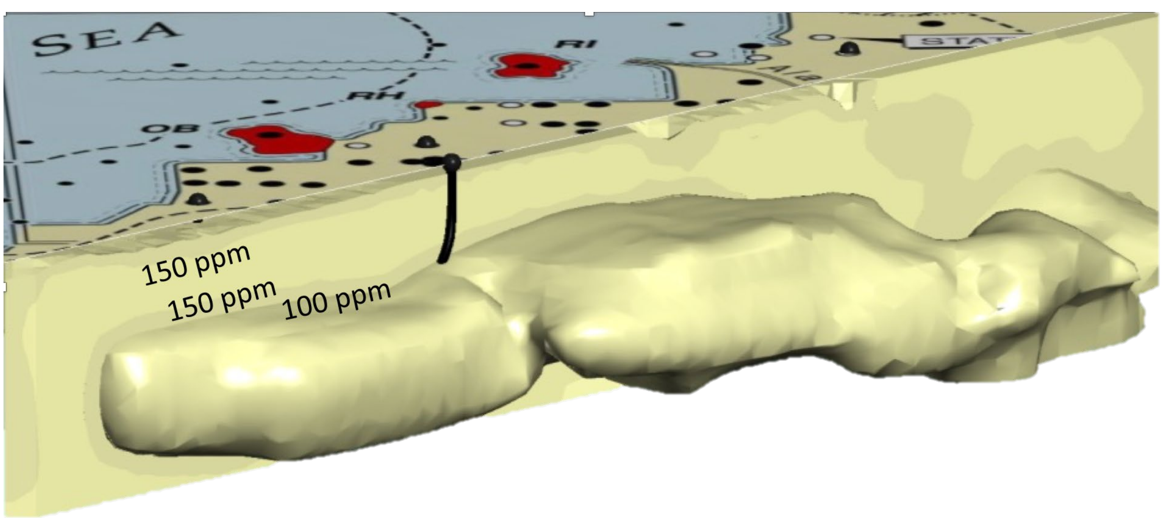

Figure 15. Future scenario model estimated lithium isosurfaces at 2043. The 150 ppm isosurface is cut away to reveal the 100 ppm isosurface.

8. Conclusions

This modeling study was a preliminary approach to characterize and forecast the recoverable lithium potential of the SSGF by building upon the existing 3D conceptual and numerical model by Araya and O’Sullivan (2022). The model has been developed using best practices to closely align with the conceptual understanding of the system’s behavior and has been calibrated to broadly match a range of observed data.

The first step was to understand the effect of salinity on the hot geothermal plume. The addition of chloride as a proxy for salinity significantly affected the thermodynamics of the system requiring substantial re-calibration of the model. While the current model is able to capture the deep hypersaline reservoir, it fails to accurately capture a less saline shallow zone. Another round of model calibration as well as increasing grid resolution should improve the match to measured chloride (and therefore lithium).

The results from this study broadly affirm the conclusions made earlier in Araya and O’Sullivan (2022) on the systems main permeability controls. The results demonstrate that the heat source is located along the Main Central Fault Zone and the faults associated with the volcanic buttes. These faults along with infield dextral faults act as major conduits for hot upflow. The dextral and redial shear faults located in the periphery act to bound the reservoir in the northwest and south. Some of these periphery dextral faults also act as large conduits for cold shallow infiltration.

The future scenario model used a simple and naïve approach to lithium extraction to generally understand the overall response of the SSGF. All the reinjected geothermal brine was assumed to have 95% of its lithium removed after 01/01/2024 and all production and reinjection rates were assumed to remain constant. We recommend testing the following more informative scenarios:

a) A staged approach to lithium removal.
b) Increased geothermal production (as planned).
c) Targeted reinjection strategy to extract lithium more efficiently.

The forecast model results show the important role connectivity between production and reinjection wells plays in determining future lithium production rates. Since the existing model is relatively coarse at 400 x 400 m in the production zone, we propose a finer refinement of 200 x 200 m or even 100 x 100 m. Model resolution in the production zone affects the accuracy of model forecasts, particularly for reinjection returns which is a key driver for forecasting lithium production rates over time. A higher resolution model will also allow us to better represent structural controls on the SSGF, improving the quality of forecasts. Lastly, we recommend uncertainty quantification of production model forecasts to account for limitations in the publicly available data.

ACKNOWLEDGMENTS

The authors would like to thank Patrick Dobson for his help in sourcing and organizing public data. His expert knowledge helped tremendously in making this study possible. We would also like to thank Kunhwi Kim for his help in organizing feedzone data, as well as his support throughout the project.

REFERENCES

Araya and O'Sullivan. "A 3D Conceptual and Natural-State Model of the Salton Sea Geothermal Field." *GRC Transactions*, 46, (2022). 2123-2155.

CalGEM. "GeoSteam: Geothermal Well Records, Production and Injection Data [Data Files]." (2022). https://geosteam.conservation.ca.gov/

California Department of Conservation. "Geological Map of California [Data File]." (2015). https://maps.conservation.ca.gov/cgs/#datalist

California Department of Conservation. "Geothermal Production and Injection Data [Salton Sea]." (2022). https://www.conservation.ca.gov/calgem/geothermal/manual

Croucher, A., O'Sullivan, M., O'Sullivan, J., Yeh, A., and Burnell, J. "Waiwera: A parallel open-source geothermal flow simulator." *Computers and Geosciences*, 141, (2020).

de Beer, A., Gravatt, M., Renaud, T., Nicholson, R., Maclaren, O. J., Dekkers, K., O'Sullivan, M., O'Sullivan, J., "Geologically Consistent Prior Parameter Distributions for Uncertainty Quantification of Geothermal Reservoirs." *48th Stanford Workshop on Geothermal Reservoir Engineering*, California, (2023).

Dekkers, K., Gravatt, M., Maclaren, O. J., Nicholson, R., Nugraha, R., O'Sullivan, M., O'Sullivan, J., "Resource Assessment: Estimating the Potential of a Geothermal Reservoir." *47th Stanford Workshop on Geothermal Reservoir Engineering*, California, (2022).

Dorsey, R. "Stratigraphy, Tectonics, and Basin Evolution in the Anza-Borrego Desert Region." In G. T. Jefferson and L. Lindsay, *Fossil Treasures of the Anza-Borrego Desert*, Sunbelt Publication, (2006) 89-104.

Dorsey, R.J., Housen, B.A., Janecke, S.U., Fanning, C.M., and Spears, A.L.F. "Stratigraphic Record of Basin Development Within the San Andreas Fault System: Late Cenozoic Fish Creek-Vallecito Basin, Southern California." *Geol. Soc. Am. Bul*., 123, (2011), 771-793.

Han, L., Hole, J.A., Stock, J.M., Fuis, G.S., Kell, A., Driscoll, N.W., Kent, G.M., Harding, A.J., Rymer, M.J., González-Fernández, A., and Lázaro-Mancilla, O. "Continental rupture and the creation of new crust in the Salton Trough rift, Southern California and northern Mexico: Results from the Salton Seismic Imaging Project." *Journal of Geophysical Research: Solid Earth*, 121, (2016), 7469-7489.

Helgeson, H.C. "Geologic and Thermodynamic Characteristics of the Salton Sea Geothermal System." *American Journal of Science*, 266, (1968), 129-166.

Hulen, J., Kaspereit, D., Norton, D.L., Osborn, W., Pulka, F.S. "Refined Conceptual Modeling and a New Resource Estimate for the Salton Sea Geothermal Field, Imperial Valley, California." *Geothermal Resources Council Transactions,* 26, (2002), 29-36.

Hulen, J., Norton, D., Kaspereit, D., Murray, L., Van de Putte, T., and Wright, M. "Geology and a Working Conceptual Model of the Obsidian Butte (Unit 6) Sector of the Salton Sea Geothermal Field, California." *GRC Transactions*, 27, (2003), 227-240.

Kaspereit, D., Mann, M., Sanyal S., Rickard, B., Osborn, W., and Hulen, J. "Updated Conceptual Model and Reserve Estimate for the Salton Sea Geothermal Field, Imperial Valley, California." *GRC Transactions*, 40, (2016), 57-66.

Kirby, S.M., Janecke, S.U., Dorsey, R.J., Housen, B.A, Langenheim, V.E., McDougall, K.A., and Steely, A.N. "Pleistocene Brawley and Ocotillo Formations: Evidence for Initial Strike-Slip Deformation Along the San Felipe and San Jacinto Fault Zones, Southern California." *Journal of Geology*, 115, (2007).

Lachenbruch, A.H., Sass, J.H., and Galanis, S.P. Jr. “Heat flow in southernmost California and the origin of the Salton Trough.” *Journal of Geophysical Research*, 90 (B8), (1985), 6709-6736.

Lynch, D.K., and Hudnut, K.W. “The Wister Mud Pot Lineament: Southeastward Extension or Abandoned Strand of the San Andreas Fault?” *Bulletin of Seismological Society of America*, 98, (2008), 1720-1729.

Marshall, S., Plesch, A., Shaw, J., and Nicholson, C. “SCEC Community Fault Model v. 5.3.2.” (2022). https://www.scec.org/research/cfm-viewer/

Mazzini, A., Svensen, H., Etiope, G., Onderrdonk, N., and Banks, D. “Fluid origin, gas fluxes and plumbing system in the sediment-hosted Salton Sea geothermal system (California, USA).” *Journal of Volcanology and Geothermal Research*, 205, (2011), 67-83.

Meidav, T., West, R., Katzenstein, A., and Rostein, Y. “An Electrical Resistivity Survey of the Salton Sea Geothermal Field, Imperial Valley California.” *Lawrence Livermore Laboratory*, UCRL-13690, (1976).

McKibben, M.A. “The Salton Trough Rift.” *SBCMA Special Publication*, 9, (1991), 76-80.

McKibben, M.A., Elders W.A., and Raju A.S.K. “Crisis at the Salton Sea: Lithium and Otherm Geothermal Mineral and Energy Resources Beneath the Salton Sea.” *Crisis at the Salton Sea: The Vital Role of Science,* University of California Riverside Salton Sea Task Force, (2021), 74-85.

McKibben, M. A., and Hardie, L. A. “Ore-forming brines in active continental rifts.” *Geochemistry of Hydrothermal Ore Deposits*, 3rd Edition, (1997), 875–933.

McKibben, M.A., Williams, A.E., Elders, W.A., and Eldridge, C.S. “Saline brines and Metallogenesis in a Modern Sediment-filled Rift: the Salton Sea Geothermal system, California, U.S.A.” *Applied Geochemistry*, 2, (1987), 563-578.

McGuire, J.J., Lohman, R.B., Catchings, R.D., Rymer, M.J., and Goldman, M.R. “Relationships Among Seismic Velocity, Metamorphism, and Seismic and Aseismic Fault Slip in the Salton Sea Geothermal Field region.” *Journal of Geophysical Research*, 120, (2015), 2600-2615.

Nichols, E. “Geothermal Exploration Under the Salton Sea Using Marine Magnetotellurics.” *California Energy Commission, PIER Renewable Energy Technologies Program*, CEC-500-2009-005, (2009).

Norton and Hulen. “Magma-Hydrothermal Activity in the Salton Sea Geothermal Field Imperial County, California.” *GRC Transactions*, 30, (2006). 991-998.

Omagbon, J., Doherty, J., Yeh, A., Colina, R., O'Sullivan, J., McDowell, J., . . . O'Sullivan, M. “Case studies of predictive uncertainty quantification for geothermal models.” *Geothermic*s. 97, (2021), 102263.

Rao, A.P. "The hydraulic connectivity, perennial warming and relationship to seismicity of the Davis-Schrimpf seep field, Salton Trough, California from new and recent temperature time-series." *M.S. thesis, California State University, Long Beach*, (2016), 107 p.

Svensen, H., Karlsen, D.A., Sturz, A., Backer-Owe, K., Banks, D.A., and Planke, S. "Processes Controlling Water and Hydrocarbon Composition in Seeps from the Salton Sea Geothermal System, California, USA." *Geology*, 35, (2007), 85-88.

O'Sullivan, M., Pruess, K., and Lippmann, M. "Geothermal Reservoir Simulation: The state-of Practice and Emerging trends." *Proceedings World Geothermal Congress*, (2000).

O'Sullivan, M., and O'Sullivan, J. "Reservoir Modeling and Simulation for Geothermal Resource Characterization and Evaluation." *Geothermal Power Generation*, (2016), 165-199.

O'Sullivan, J., Popineau, J., Gravatt, M., Renaud, T., Riffault, J., Croucher, A., Yeh, A. & O'Sullivan M. "An integrated, mesh-independent geothermal modeling framework." *Environmental Modeling and Software*, 163, (2023), 105666.

Palmer, T.D. "Characteristics of Geothermal Wells Located in the Salton Sea Geothermal Field, Imperial County, California." *Lawrence Livermore Laboratory,* UCRL-51976, (1975).

Popineau, J., O'Sullivan, J., O'Sullivan, M., Archer, R., and Williams, B. "An integrated Leapfrog /TOUGH2 Workflow for a Geothermal Production Modeling." *7th African Rift Geothermal Conference*, (2018).

Sass, J.H., Galanis, S.P., Jr., Lachenbruch, A.H., Marshall, B.V., and Munroe, R.J. "Temperature, Thermal Conductivity, Heat Flow, and Radiogenic Heat Production from Unconsolidated Sediments of the Imperial Valley, California." *USGS Open File Report*, 84-490, (1984).

Sass, J.H., Priest, S.S., Duda, L.E., Carson, C.C., Hendricks, J.D., and Robison, L.C. "Thermal Regime of the State 2-14 well, Salton Sea Scientific Drilling Project." *Journal of Geophysical Research*, 93 (B11), (1988), 12,995-13,004.

Williams, A.E., and McKibben, M.A. "A Brine Interface in the Salton Sea Geothermal System California: Fluid Geochemical and Isotopic Characteristics." *Geochimica et Cosochimica Acta*, 53, (1989), 1905-1920.

Younker, L.W., Kasameyer, P.W., and Tewhey, J.D. "Geological, Geophysical, and Thermal Characteristics of the Salton Sea Geothermal Field, California." *Journal of Volcanology and Geothermal Research*, 12, (1981), 221-258.